

## EXPLORING THE CONNECTION BETWEEN PARSEC-SCALE JET ACTIVITY AND BROADBAND OUTBURSTS IN 3C 279

B. RANI<sup>1</sup>, S. G. JORSTAD<sup>2,7</sup>, A. P. MARSCHER<sup>2</sup>, I. AGUDO<sup>3</sup>, K. V. SOKOLOVSKY<sup>4,5,6</sup>, V. M. LARIONOV<sup>7,8</sup>, P. SMITH<sup>9</sup>, D. A. MOSUNOVA<sup>5</sup>, G. A. BORMAN<sup>10</sup>, T. S. GRISHINA<sup>7</sup>, E. N. KOPATSKAYA<sup>7</sup>, A. A. MOKRUSHINA<sup>7,8</sup>, D. A. MOROZOVA<sup>7</sup>, S. S. SAVCHENKO<sup>7</sup>, YU. V. TROITSKAYA<sup>7</sup>, I. S. TROITSKY<sup>7</sup>, C. THUM<sup>11</sup>, S. N. MOLINA<sup>3</sup>, C. CASADIO<sup>12,3</sup>

<sup>1</sup>NASA Goddard Space Flight Center, Greenbelt, MD, 20771, USA

<sup>2</sup>Institute for Astrophysical Research, Boston University, 725 Commonwealth Avenue, Boston, MA 02215, USA

<sup>3</sup>Instituto de Astrofísica de Andalucía (CSIC), Apartado 3004, E-18080 Granada, Spain

<sup>4</sup>IAASARS, National Observatory of Athens, Vas. Pavlou & I. Metaxa, GR-15 236 Penteli, Greece

<sup>5</sup>Astro Space Center of Lebedev Physical Institute, Profsoyuznaya St. 84/32, 117997 Moscow, Russia

<sup>6</sup>Sternberg Astronomical Institute, Moscow State University, Universitetskii pr. 13, 119992 Moscow, Russia

<sup>7</sup>Astron. Inst., St.-Petersburg State Univ., Russia

<sup>8</sup>Pulkovo Observatory, St.-Petersburg, Russia

<sup>9</sup>Steward Observatory, University of Arizona, Tucson, AZ 85721, USA

<sup>10</sup>Crimean Astrophysical Observatory, P/O Nauchny, Crimea, 298409, Russia

<sup>11</sup>Instituto de Radio Astronomía Millimétrica, Avenida Divina Pastora, 7, Local 20, E-18012 Granada, Spain and

<sup>12</sup>Max-Planck-Institut für Radioastronomie, Auf dem Hügel, 69, D-53121, Bonn, Germany

*Draft version May 22, 2018*

### ABSTRACT

We use a combination of high-resolution very long baseline interferometry (VLBI) radio and multi-wavelength flux density and polarization observations to constrain the physics of the dissipation mechanism powering the broadband flares in 3C 279 during an episode of extreme flaring activity in 2013-2014. Six bright flares superimposed on a long-term outburst are detected at  $\gamma$ -ray energies. Four of the flares have optical and radio counterparts. The two modes of flaring activity (faster flares sitting on top of a long term outburst) present at radio, optical,  $\gamma$ -ray frequencies are missing in X-rays. X-ray counterparts are only observed for two flares. The first three flares are accompanied by ejection of a new VLBI component (NC2) suggesting the 43 GHz VLBI core as the site of energy dissipation. Another new component, NC3, is ejected after the last three flares, which suggests that the emission is produced upstream from the core (closer to the black hole). The study therefore indicates multiple sites of energy dissipation in the source. An anti-correlation is detected between the optical percentage polarization (PP) and optical/ $\gamma$ -ray flux variations, while the PP has a positive correlation with optical/ $\gamma$ -rays spectral indices. Given that the mean polarization is inversely proportional to the number of cells in the emission region, the PP vs. optical/ $\gamma$ -ray anti-correlation could be due to more active cells during the outburst than at other times. In addition to the turbulent component, our analysis suggests the presence of a combined turbulent and ordered magnetic field, with the ordered component transverse to the jet axis.

*Subject headings:* galaxies: active – quasars: individual: 3C 279 – radio continuum: galaxies – jets: galaxies – gamma-rays

### 1. INTRODUCTION

Combined information from the high-resolution images obtained using very long baseline interferometry (VLBI) radio and broadband intensity variations has been proven to be one of the most useful approaches to locate and to probe the high-energy radiation processes in blazars – Active Galactic Nuclei (AGN) in which one of the jets points close to our line of sight. Investigation of intensity variations in individual sources in combination with the VLBI component ejection/kinematics indicates that high-energy emission is associated with the compact regions in relativistic jets (e.g. Agudo et al. 2011; Jorstad et al. 2010; Marscher 2008; Rani et al. 2014, 2015, 2016, and references therein). A recent study for blazar S5 0716+714 by Rani et al. (2014) reported a significant correlation between the  $\gamma$ -ray flux and the direction of the jet outflow variations. This study implies a causal connection between the jet morphology and the observed  $\gamma$ -ray flares.

We present here an investigation of parsec-scale jet mor-

phology evolution in the blazar 3C 279 during an episode of extreme flaring activity at GeV energies in 2014, using 43 GHz VLBI images. The focus of this study is to explore the total intensity and polarization properties and their connection with the broadband flux variations observed during this bright  $\gamma$ -ray activity phase of the source.

The flat spectrum radio quasar (FSRQ) 3C 279, at a redshift of  $z = 0.538$  (Burbidge & Rosenberg 1965), has a black hole mass in the range of  $(3-8) \times 10^8 M_{\odot}$  (Woo & Urry 2002; Gu et al. 2001). 3C 279 has a bright jet extending up to kiloparsec scales (Cheung 2002) and exhibits a range of apparent velocities from 4 to  $20 c$  (Lister et al. 2013). The parsec scale jet is aligned close to the observer's line of sight ( $\leq 2^{\circ}$ , Lister et al. 2013; Jorstad et al. 2004). Because of its strong optical polarization and flux variability, 3C 279 is often classified as an optically violently variable (OVV) quasar. Polarimetric observations have detected both linearly and circularly polarized emission from the parsec-scale jet of 3C 279 (Wardle et al. 1998; Taylor 2000; Homan et al. 2009). Moreover, the observed radiation at optical frequencies is also highly polarized in the source e.g. an ob-

served value of 45.5% in optical U band (Mead et al. 1990). Wagner & Mannheim (2001) detected variable optical circular polarization in 3C 279 exceeding 1%.

With its high flux density and prominent variations in total intensity and polarization, 3C 279 has been the subject of several intensive multi-wavelength campaigns (e.g., Maraschi et al. 1994; Hartman et al. 1996; Chatterjee et al. 2008; Wehrle et al. 1998; Larionov et al. 2008; Collmar et al. 2010; Böttcher et al. 2007; Hayashida et al. 2012, 2015; Kang et al. 2015). In particular, prominent  $\gamma$ -ray flares were recorded in the source by the Energetic Gamma-Ray Experiment Telescope (EGRET) on board the *Compton Gamma-Ray Observatory* (CGRO) (Hartman et al. 1992), and the *Fermi*/LAT (Large Area Telescope) has detected the source regularly since its launch in 2008 (Abdo et al. 2010). In 2006, the Major Atmospheric Gamma-Ray Imaging Cherenkov (MAGIC) telescope observed TeV ( $E > 200$  GeV) emission from the source (Albert et al. 2008). In December 2013, the source went through a series of extremely rapid  $\gamma$ -ray flares reaching a flux level  $F$  ( $E > 100$  MeV) of  $10^{-5}$  photons  $\text{cm}^{-2} \text{s}^{-1}$  on timescales of the order of a few hours (Hayashida et al. 2015). In June 2015, record-breaking flaring activity was observed (Cutini 2015) with the highest measured flux,  $F$  ( $E > 100$  MeV) of  $3.6 \times 10^{-5}$  photons  $\text{cm}^{-2} \text{s}^{-1}$  (Ackermann et al. 2016).

This paper is structured as follows. Section 2 provides a brief description of observations and data reduction. In Section 3, we report and discuss our results. Finally, summary and conclusions are given in Section 4. Throughout this paper we adopted a  $\Lambda$ CDM cosmology with  $\Omega_m = 0.27$ ,  $\Omega_\lambda = 0.73$ , and  $H_0 = 71 \text{ km s}^{-1} \text{ Mpc}^{-1}$  (Spergel et al. 2003). At a redshift of 0.538, the luminosity distance  $d_L$  is 3085 Mpc and an angular separation of 1 milli-arcsecond (mas) translates into a linear distance of 6.32 pc.

## 2. MULTIFREQUENCY DATA: OBSERVATIONS AND DATA REDUCTION

From November 01, 2013 to August 30, 2014, the broadband flaring activity of the FSRQ 3C 279 was extensively covered using both ground- and space- based observing facilities. The following sub-sections summarize the observations and data reduction.

### 2.1. VLBA Observations

The 7 mm VLBA observations of the source were obtained in the course of a program<sup>1</sup> of monthly monitoring of bright  $\gamma$ -ray blazars at 43 GHz. The details of the observations can be found in Jorstad et al. (2017). The data reduction is performed using the Astronomical Image Processing System (AIPS) and Difmap (Shepherd 1997). Details of the data reduction are described in Jorstad et al. (2005, 2017). We model-fit the brightness distribution of the source using circular Gaussian components using Difmap, and the model-fit parameters (peak flux density, distance from (0,0) co-ordinates, position angle, and size) are listed in the Table 2 in Appendix. The polarization parameters (polarized flux density and electric vector position angle, EVPA) are determined by model-fitting the Stokes Q and U in  $(u, v)$  data. The polarized flux density is given by  $\sqrt{Q_{\text{flux}}^2 + U_{\text{flux}}^2}$  and the EVPA by  $0.5 \times \arctan(U_{\text{flux}}/Q_{\text{flux}})$ .

### 2.2. Radio observations

The 230 and 345 GHz data are provided by the Submillimeter Array (SMA) Observer Center<sup>2</sup> data base (Gurwell et al. 2007). The 230 GHz total flux density data are complemented by the data from the POLAMI (Polarimetric Monitoring of Active Galactic Nuclei at Millimetre Wavelengths) Program<sup>3</sup> (Agudo et al. 2018b,a; Thum et al. 2018). POLAMI is a long-term program to monitor the polarimetric properties (Stokes I, Q, U, and V) of a sample of around 40 bright AGN at 3.5 and 1.3 millimeter wavelengths with the IRAM 30m Telescope near Granada, Spain. The program has been kept running since October 2006, and it currently has a time sampling of  $\sim 2$  weeks. The XPOL polarimetric observing setup has been routinely used as described in Thum et al. (2008) since the start of the program. The reduction and calibration of the POLAMI data presented here are described in detail in Agudo et al. (2010, 2014, 2018b). We also make use of the 15 GHz OVRO (Owens Valley Radio Observatory) data publicly available at the OVRO website<sup>4</sup>. Details of observations and data reduction are described in Richards et al. (2011).

### 2.3. Optical observations

During our campaign period, the source was simultaneously observed in 6 optical/UV filters (U, B, V, W1, W2, and M2) by *Swift*/UVOT (Romig et al. 2005). We used the *uvotsource* tool from HEASoft v6.16 for the data analysis (Poole et al. 2008). A step-by-step data reduction procedure is described in Rani et al. (2017) to which we refer for details. We have also included optical/IR data at B, V, R, J, and K passbands from the Small and Moderate Aperture Research Telescope System (SMARTS5) monitoring program. The reduction and analysis of this data is described in Bonning et al. (2012).

We also make use of the optical R passband flux and polarization observations provided by the Steward observatory blazar monitoring program<sup>5</sup>; the details of observations and data reduction are described in Smith (2016). Additional optical R band polarimetric observations were obtained at the 1.83 m Perkins telescope of the Lowell Observatory (Flagstaff, AZ) using the PRISM camera<sup>6</sup>. The details of observations and data reduction are given in Jorstad & Marscher (2016). We also used polarimetric and photometric data from the AZT-8 (Crimean Astrophysical Observatory) and LX-200 (St. Petersburg, Russia) telescopes. The details of observations and data reductions are given in Larionov et al. (2008).

Finally, data were corrected for the Galactic extinction using the coefficients of Schlegel et al. (1998) for different filters<sup>7</sup>. We converted the magnitudes to fluxes using the central wavelengths for each filter as calibrated by Poole et al. (2008) for the space-based observations. For ground-based observations, the zero-point fluxes<sup>8</sup> corresponding to the observed wavelengths were used for magnitude to flux conversion.

### 2.4. X-ray observations

X-ray observations (0.3 – 10 keV) of the source were obtained using the *Swift*/XRT telescope (Burrows et al. 2005)

<sup>2</sup> <http://sma1.sma.hawaii.edu/callist/callist.html>

<sup>3</sup> <https://polami.iaa.es>

<sup>4</sup> <http://www.astro.caltech.edu/ovroblazars/>

<sup>5</sup> <http://james.as.arizona.edu/~psmith/Fermi/>

<sup>6</sup> [www.bu.edu/prism/](http://www.bu.edu/prism/)

<sup>7</sup> search for 3C 279 at <http://ned.ipac.caltech.edu/>

<sup>8</sup> <http://ssc.spitzer.caltech.edu/warmmission/propkit/pet/magtojy/ref.html>

<sup>1</sup> VLBA-BU-BLAZARS, <http://www.bu.edu/blazars>

both in the photon counting and windowed timing mode. The data are analyzed using the standard `xrtpipeline v0.13.2`. The spectra in individual time bins were modeled with `XSPEC v12.9.0` to extract the photon counts and indices. We used the absorbed power law with the total HI column density fixed to the Galactic value ( $N_{HI} = 0.212 \times 10^{21}$ , Kalberla et al. 2005) to model the 0.3 – 10 keV spectrum, which provided an acceptable fit at all epochs. The details of the observations and data reduction are discussed in Rani et al. (2017).

### 2.5. Gamma rays

We employed here the 100 MeV – 300 GeV data of the source observed in survey mode by the *Fermi*-LAT (Large Area Telescope, Atwood et al. 2009). The LAT data were analyzed using the standard `ScienceTools` (software version `v10.r0.p5`) and instrument response function `P8R2_SOURCE_V6`. Photons in the Source event class were selected for the analysis. We analyzed a region of interest (ROI) of  $20^\circ$ , centered at the position of 3C 279 using a maximum-likelihood algorithm (Mattox et al. 1996). For the unbinned likelihood analysis<sup>9</sup>, all 3FGL (Acero et al. 2015) sources within the ROI were included. We also included the Galactic diffuse background (`gll_l1em_v06.fits`) and the isotropic background (`iso_P8R2_SOURCE_V6_v06.txt`) emission components<sup>10</sup>. Model parameters for sources within  $5^\circ$  of the center of the ROI were kept free. Model parameters for variable sources (variability index  $\geq 72.44$  in the 3FGL catalog) were also set free while the model parameters of non-variable sources beyond  $5^\circ$  were fixed to their catalog values.

To characterize the variability properties of the source, we computed the photon flux light curve of the source at E above  $E_0$ , where  $E_0$  is the de-correlation energy (Lott et al. 2012), which minimizes the correlations between integrated photon flux and photon index. During our campaign, we obtain  $E_0 = 219$  MeV. We generated the constant uncertainty (15%) light curve above  $E_0$  through the adaptive binning method following Lott et al. (2012). The bin size ranges between 0.07 to 31.06 days with an average of 5.43 days. The adaptive binned light curve is produced by modeling the spectra by a simple power law,  $N(E) = N_0 E^{-\Gamma}$ ,  $N_0$  : prefactor, and  $\Gamma$  : power-law index.

## 3. RESULTS AND DISCUSSION

This section presents the light curve analysis – flux and polarization variability at different energy bands and the evolution of the jet brightness. We also investigate the connection between jet kinematics and broadband flaring activity.

### 3.1. Observed outburst and its multi-frequency behavior

The observed broadband flux density variations in 3C 279 during a major  $\gamma$ -ray outburst are plotted in Fig. 1. The source became active at GeV energies in early November 2013, and the flaring activity continued until August 2014. Hereafter we will use  $JD'$  (defined as  $JD - 2455000$ ) for time. In Fig. 1, the cyan dashed lines labeled as “A” and “D” mark the beginning and end of the outburst, respectively. The source displayed multiple flares across the whole electromagnetic spectrum over this period, which we visually inspected and labeled as follows. The blue dotted-dashed lines (“1” to “6”)

are marked close to the peak of the rapid  $\gamma$ -ray flares labeling the broadband flares as “G” for  $\gamma$ -rays, “X” for X-rays, “O” for optical, “R” for radio followed by the number. For instance, the  $\gamma$ -ray flares should be read as G1 to G6.

Flare 2 is observed close in time at  $\gamma$ -ray and X-ray energies. The first two flares are accompanied by an increase in the source brightness at radio frequencies. At optical frequencies (panel c) the source is still in quiescent phase. The peak of flare G3 coincides with a minimum in the X-ray light curve, but has optical and radio counterparts and a delayed response in X-rays. In comparison to X1 and X2, X3 has a rather low magnitude. Because of the gap in observations at X-ray energies, it is hard to determine the absence/presence of an X-ray counterpart for flare G4, but the flare has a near-simultaneous optical and radio counterpart. A prominent optical flare (labeled as 3.5) is seen between flare 3 and 4. The flare O3.5 is accompanied by similar activity at radio (230 GHz) band; however, the observed variations are quite mild at X-ray and  $\gamma$ -ray energies. Flare 5 is the only one that is observed quasi-simultaneously at all energies (radio to  $\gamma$ -rays). Flare 5 has a double feature in  $\gamma$ -rays and X-rays (see Figs. 2 and 4).

The other two interesting states in the broadband activity are marked as “B” and “C”. After the first five  $\gamma$ -ray flares, a local minimum (“B”) is observed simultaneously at all frequencies. The local minimum was followed by a concurrent flare (flare 6) at radio, optical,  $\gamma$ -ray energies; no significant activity was observed in the X-ray regime during this period. Period “C” marks the end of flare 6, which happened to be almost simultaneous for all light curves. A continuous decay in the source brightness was observed between period C and D, which we refer to as the post-outburst plateau.

#### 3.1.1. Gamma-ray Variability

Figure 2 displays details of the observed  $\gamma$ -ray flaring activity of 3C 279. The rapid flares (labeled as 1 to 6) were superimposed on top of a broad outburst. The source started to brighten from a flux level  $F$  ( $E > 219$  MeV)  $\sim 3.3 \times 10^{-7}$  photons  $\text{cm}^{-2} \text{s}^{-1}$  on  $JD' \sim 1610$  and returned to the same brightness level on  $JD' \sim 1850$ . The solid green line in Fig. 2 marks the observed brightness level ( $\sim 3.3 \times 10^{-7}$  photons  $\text{cm}^{-2} \text{s}^{-1}$ ) of the source before and after the outburst period. Significant variations in  $\gamma$ -ray photon index were observed during this period. The estimated  $\Gamma$  value is 2.7 at the beginning and end of the outburst. A significant spectral variation is observed for the individual flares (1 to 6). For each flare, the spectrum gets harder at the peak, and later it softens again. The fastest observed  $\gamma$ -ray flare during this activity period had a flux-doubling time scale of  $\sim 2$  hrs and a very hard  $\gamma$ -ray spectrum with  $\Gamma = 1.7$  (Hayashida et al. 2015).

In Fig. 3, we plot the  $\gamma$ -ray photon flux values as a function of photon index. A clear spectral hardening with an increase in source brightness can be seen here. Since we investigate the correlation above the de-correlation energy ( $E_0$ ), the estimated correlation is not sensitive to the LAT instrumental bias. A Pearson correlation analysis reveals a significant correlation between the two. Formally, we obtained  $r_P^{11} = -0.33$  and a p-value = 0.0019, which suggests a significant anti-correlation at a confidence level of  $>99\%$ . It is therefore evident that not only the major outburst but also the individual  $\gamma$ -ray flares are characterized by significant spectral hardening although with substantial scatter.

<sup>9</sup> [http://fermi.gsfc.nasa.gov/ssc/data/analysis/scitools/likelihood\\_tutorial.html](http://fermi.gsfc.nasa.gov/ssc/data/analysis/scitools/likelihood_tutorial.html)

<sup>10</sup> <http://fermi.gsfc.nasa.gov/ssc/data/access/lat/BackgroundModels.html>

<sup>11</sup>  $r_P$  is the linear Pearson correlation coefficient and p-value is the probability of the null hypothesis

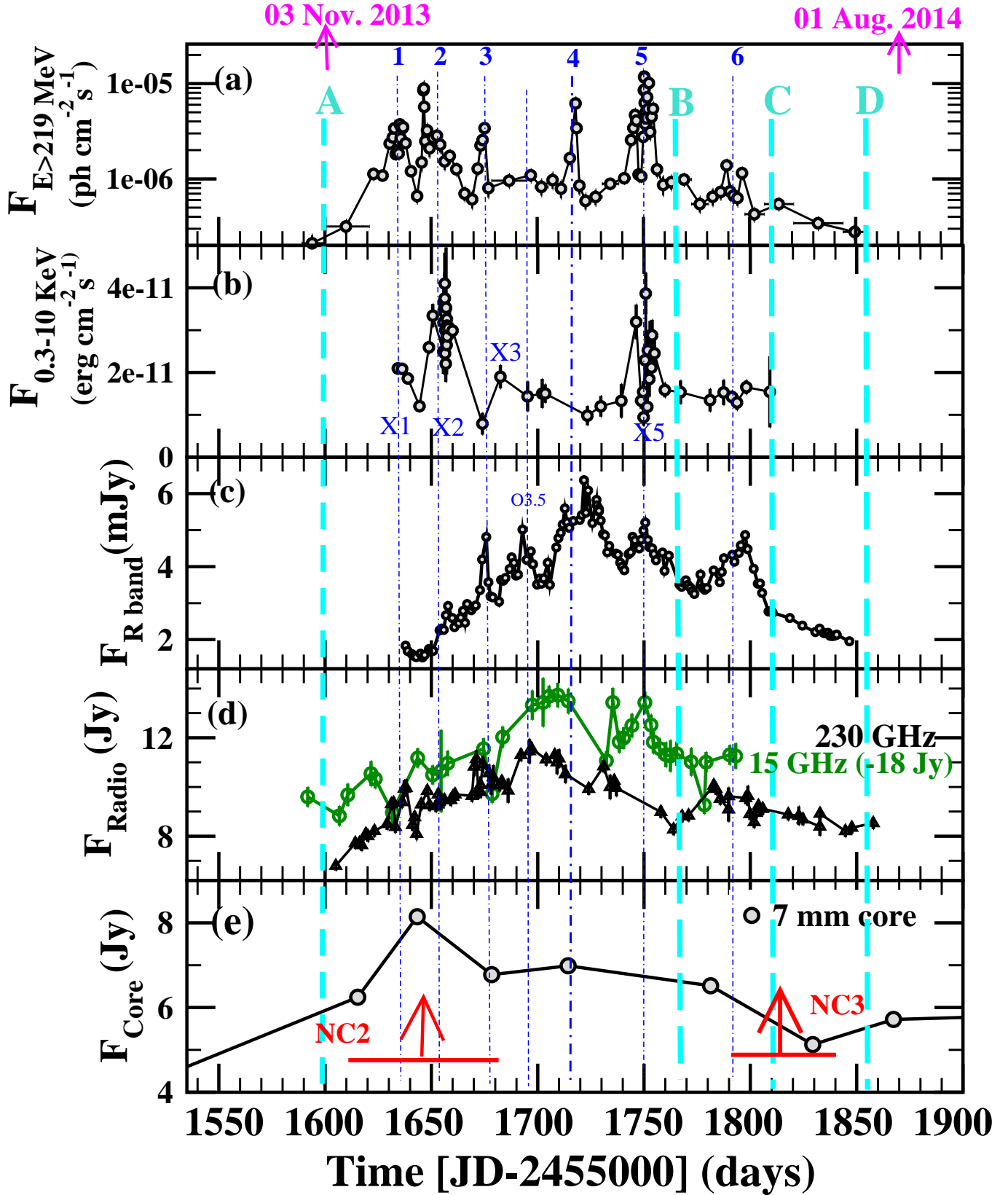


FIG. 1.— Broadband flux light curves of 3C 279: (a)  $\gamma$ -ray light curve at  $E>219$  MeV; (b) X-ray light curve at 0.3-10 keV; (c) optical R passband light curve, (d) 230 and 15 GHz radio flux density light curves, and (e) flux density variations in the 7 mm VLBI core. The red arrows mark the ejection times of new components (see Sect. 3.3 for details). As for other figures hereafter, the cyan dashed lines (labelled as A to D) represent the different flaring activity states of the source (see Sect. 3.1 for more details). The peaks of the rapid  $\gamma$ -ray flares (1 to 6) are marked with the blue dotted-dashed lines. The orange dashed line shows the time of an optical flare (3.5) that has no obvious counterparts at other wavelengths. In all cases, lines connecting the data points are simply to guide the eye.

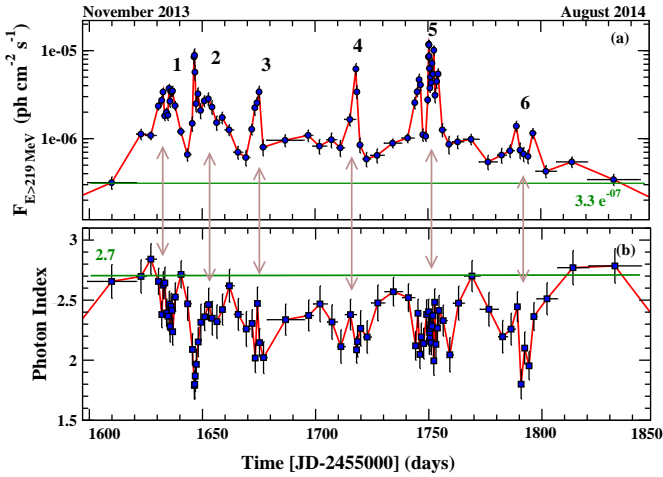


FIG. 2.— Gamma-ray photon flux (top) and photon index (bottom) light curves of 3C 279. The bright  $\gamma$ -ray flare and the corresponding spectral variations are shown with the gray arrows. The photon flux and photon index values at the beginning and end of the outburst are marked with the green lines.

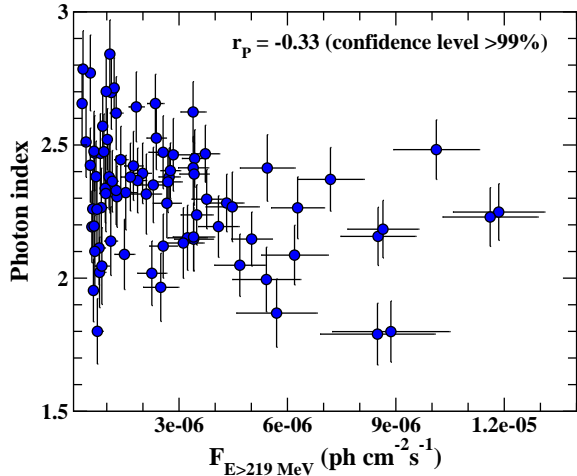


FIG. 3.— Gamma-ray photon index vs. photon flux for  $E > 219$  MeV.

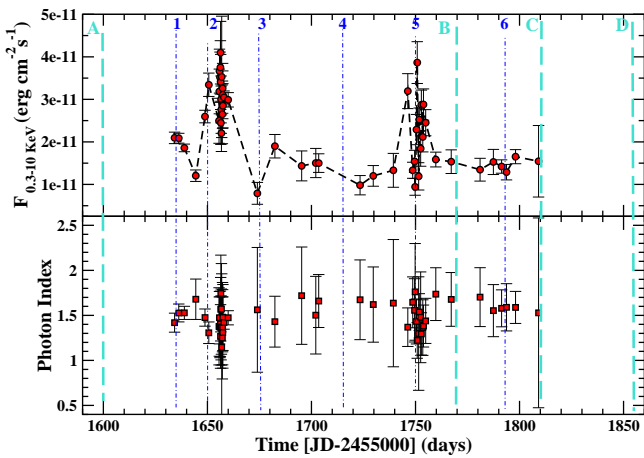


FIG. 4.— Energy flux (top) and photon index (bottom) light curves of 3C 279 at 0.3–10 KeV X-ray bands (vertical dotted and dashed lines are same as in Fig. 1).

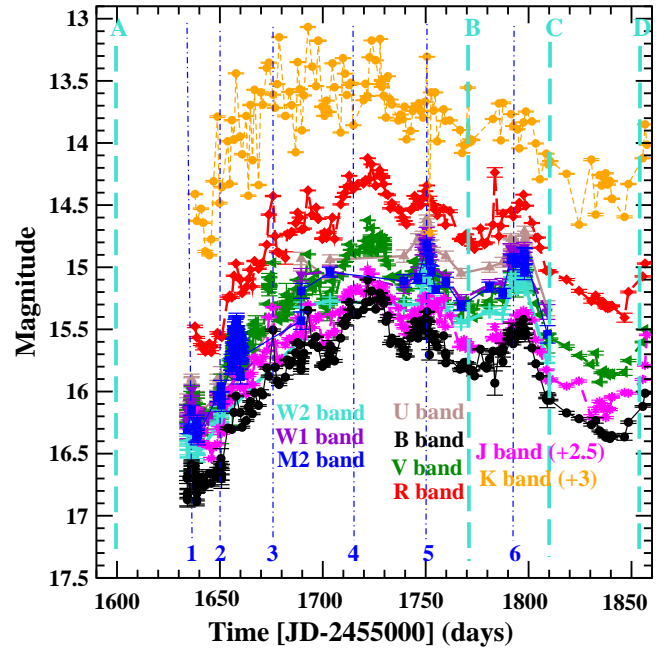


FIG. 5.— Near-IR (J and K), UV (W1, W2, and M2), and optical (U, B, V, and R) light curves of 3C 279 (vertical dotted and dashed lines are same as in Fig. 1).

### 3.1.2. X-ray Variability

The X-ray energy flux and photon index light curves are shown in Fig. 4. Compared to the  $\gamma$ -ray light curve, the X-ray observations were rather sparse. We could identify two prominent flares in the X-ray light curve. Apparently, the first X-ray flare coincides with flare G2 in  $\gamma$  rays and the second X-ray flare with flare G5. While the X-ray energy flux is varying by a factor of more than four, the photon index remains consistent with the mean value of  $\Gamma_X = 1.47 \pm 0.01$ .

### 3.1.3. Variability at Optical frequencies

The observed near-IR, optical, and UV light curves of the source are shown in Fig. 5. Similar to  $\gamma$ -rays, there are two modes of flaring activity at optical frequencies. Fast flares (timescale  $\sim 20$ -30 days) are superimposed on the broad outburst. No optical observations are available before  $\text{JD}' = 1635$  (December 2013). The flaring behavior is very similar for the near-IR, optical, and UV light curves.

The average IR-optical-UV (hereafter IOU) spectrum over the entire period of our observations is shown in Fig. 6 (top). The observed IOU spectrum is steep until an upturn at UV frequencies. The excess emission could be due to thermal dominance either from the accretion disk or broad-line region. The observed IOU spectrum can be well described by a power law,  $F(\nu) \propto \nu^{-\alpha}$ , where  $\alpha$  is the spectral index. For the average spectrum, we obtained  $\alpha = 1.91 \pm 0.08$ .

To investigate the spectral variations during the broad outburst, we constructed the IOU spectrum every 20 days. The spectral index is estimated via fitting the spectrum by a power law as described above. Prominent variations in the IOU spectral indices can be seen in Fig. 6 (bottom). The IOU spectrum is steeper at the beginning of the outburst ( $\alpha_{IOU} \sim 2$ , Flare 2), and the spectrum gets harder as the source brightness increases. The estimated  $\alpha_{IOU}$  is  $\sim 1.6$  (Flare 6) at the peak of the outburst ( $\text{JD}' \sim 1720$ ). However, the spectral variations are quite marginal during the decay phase of the outburst, with  $\alpha_{IOU}$  remaining nearly consistent with a value of  $\sim 1.6$ .

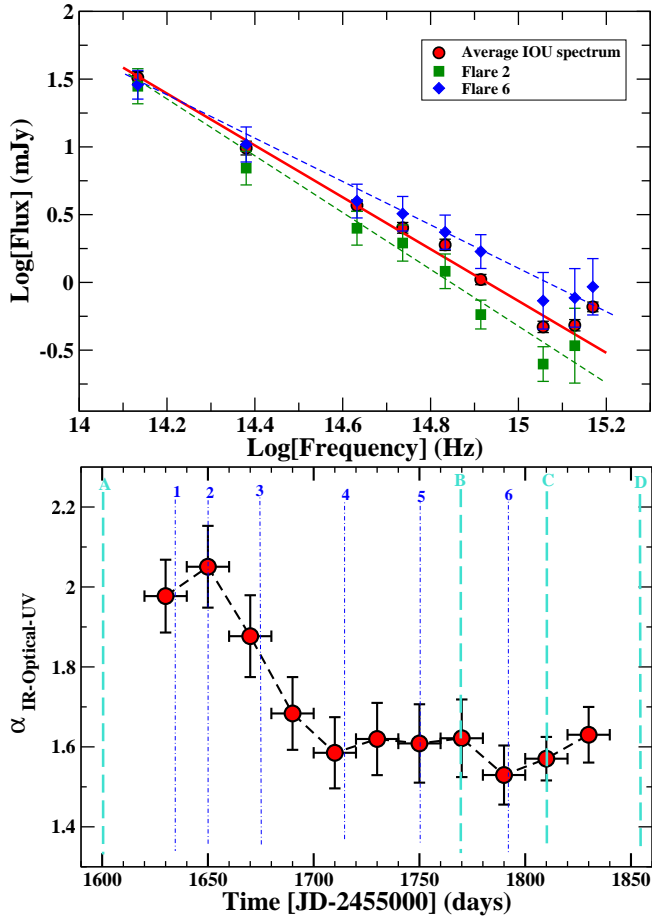


FIG. 6.— Top: Average IOU spectrum (data points are the mean values and the error bars representation their standard deviation) of 3C 279 over the entire period of observations, and a change in spectral index from  $\sim 2$  (Flare 2 in green) to  $\sim 1.6$  (Flare 6 in blue). Bottom: Spectral index variations (vertical dotted and dashed lines are same as in Fig. 1).

Figure 7 presents the optical polarization variations observed in the source. The fractional polarization drops from  $\sim 25\%$  to  $\sim 5\%$  within the first 50 days of our observations; this period coincides with the beginning of the  $\gamma$ -ray outburst. The sharp drop in percentage polarization was followed by a slow rise (superimposed with rapid variations) until August 2014. At the end of the outburst in August 2014, the percentage polarization returned to its original value of  $\sim 25\%$ . The optical polarization angle (EVPA,  $\chi$ ) variations on the other hand are quite modest ( $\Delta\chi \sim 60^\circ$ ). Throughout the campaign period, EVPA remained consistent with an average value of  $\sim 50^\circ$ , which is along the parsec-scale jet direction of  $\sim -135^\circ$  (Jorstad et al. 2017).

### 3.1.4. Variability at Radio frequencies

In Fig. 8, we plot the radio flux density light curves sampled at 15, 86, 230, and 350 GHz bands. The observed variations appear quite similar at 15 and 230 GHz bands, the most densely sampled frequencies. Faster variations (for instance the flare between 3 and 4) superimposed on the broad outburst can be seen here. A prominent flare is also apparent in the 86 GHz light curve; however data sampling is quite sparse close to the peak of the outburst. The data sampling is even worse at the 350 GHz, and as a result the flaring activity is less evident.

The percentage polarization (top) and EVPA (bottom)

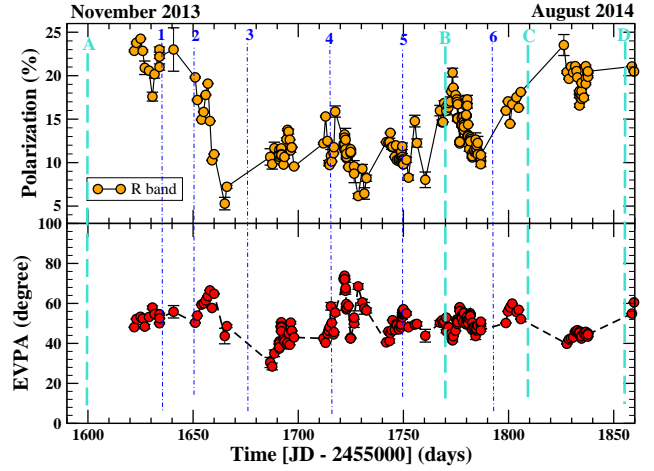


FIG. 7.— Optical R band percentage polarization and EVPA variations (vertical dotted and dashed lines are same as in Fig. 1).

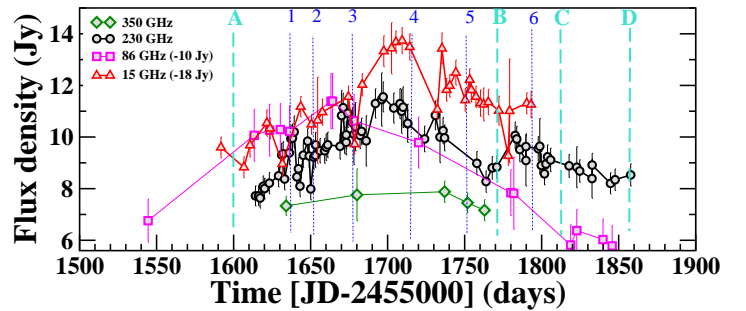


FIG. 8.— Flux density light curves at 15, 86, 230, and 350 GHz radio bands (vertical dotted and dashed lines are same as in Fig. 1). The 15 GHz and 86 GHz data shifted by  $-18$  Jy and  $-10$  Jy, respectively.

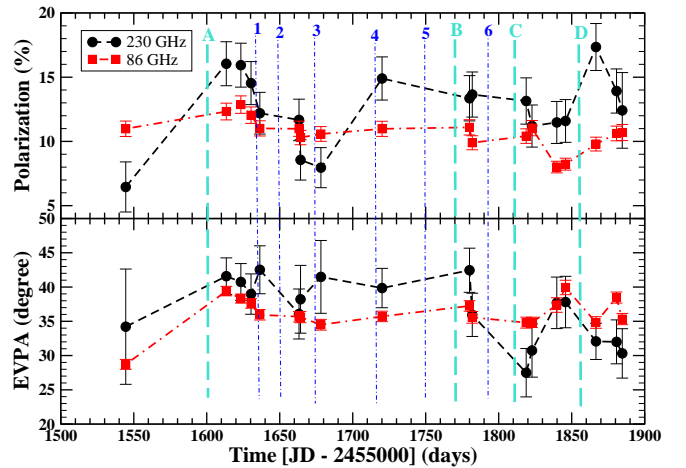


FIG. 9.— Percentage polarization (top) and EVPA curves at 86 (in red) and 230 GHz (in black) bands (vertical dotted and dashed lines are same as in Fig. 1).

curves at 86 and 230 GHz radio bands are shown in Fig. 9. There are significant variations in the 230 GHz band percentage polarization curve. For instance, the percentage polarization drops from 15% to 5% between  $\text{JD}' = 1600$  and 1700, and it increases again to 15% at  $\text{JD}' \sim 1720$ . The observed polarization was quite high ( $\sim 15\%$ ) for the rest of the period. On the other hand, the percentage polarization variations at 86 GHz band and the EVPA variations at both 86 and 230 GHz bands were quite modest ( $\Delta\chi \leq 25^\circ$ ).

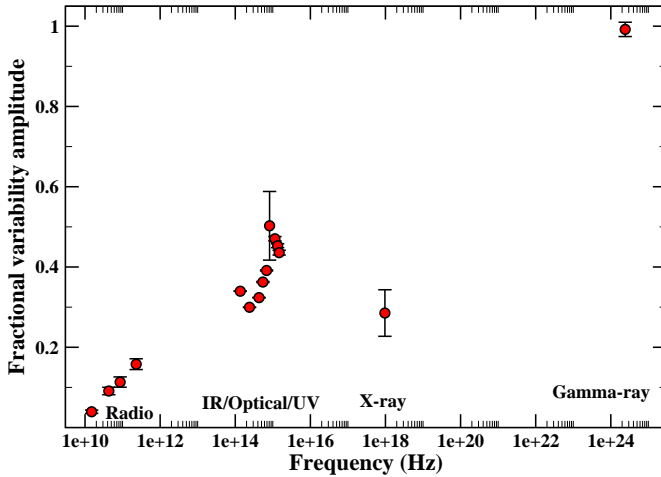


FIG. 10.— Fractional variability amplitudes of 3C 279 from radio to  $\gamma$ -ray energies.

### 3.2. Light curve analysis

#### 3.2.1. Fractional Variability

To quantify how the amplitude of flux variations changes as a function of frequency, we compared the fractional variability amplitude ( $F_{var}$ ) of the observed light curves. For a given light curve with an average flux  $\bar{x}$  and sample variance  $S^2$ ,  $F_{var}$  is defined as (Vaughan et al. 2003):

$$F_{var} = \sqrt{\frac{S^2 - \overline{\sigma_{err}^2}}{\bar{x}^2}} \quad (1)$$

where  $\overline{\sigma_{err}^2}$  is the mean of the squared measurement uncertainties. The uncertainty on  $F_{var}$  due to the measurement-error fluctuations was derived through Monte Carlo simulations by Vaughan et al. (2003, eq. B2).

Figure 10 shows the calculated  $F_{var}$  at different frequencies. A gradual increase in  $F_{var}$  with frequency is visible in the radio regime, and this trend continues until the IOU regime. The first peak in the  $F_{var}$  vs. frequency curve is observed at the optical U passband, which is followed by a dip in the X-ray regime. Compared to the lower frequencies, the  $F_{var}$  is extremely large at  $\gamma$ -rays;  $F_{var} > 1$  implies more than 100% variations.

#### 3.3. Parsec scale jet Kinematics

In Fig. 11, we display an example image of the 3C 279 jet. The top panel shows the circular Gaussian components (yellow crossed-circles) superimposed on top of the total intensity contours. The bottom panel shows the composite super-resolved image convolved with a beam size of 0.1 mas (0.63 parsec). In the composite image, the contours represent the total intensity and the color scale represents the polarized intensity. The yellow line segments mark the EVPA direction.

The total intensity of the jet is described using circular Gaussian components, and we list the model fit parameters in Table 2 in Appendix. To study the evolution of flux density and polarization of components, and also the component motion and their evolution as a function of time, we cross-identify the features using the following assumption. We assumed that the changes in the flux density, distance from the VLBI core, position angle, and size should be small for the time period between adjacent epochs to prevent a potentially large systematic error arising from the incorrect cross-identification.

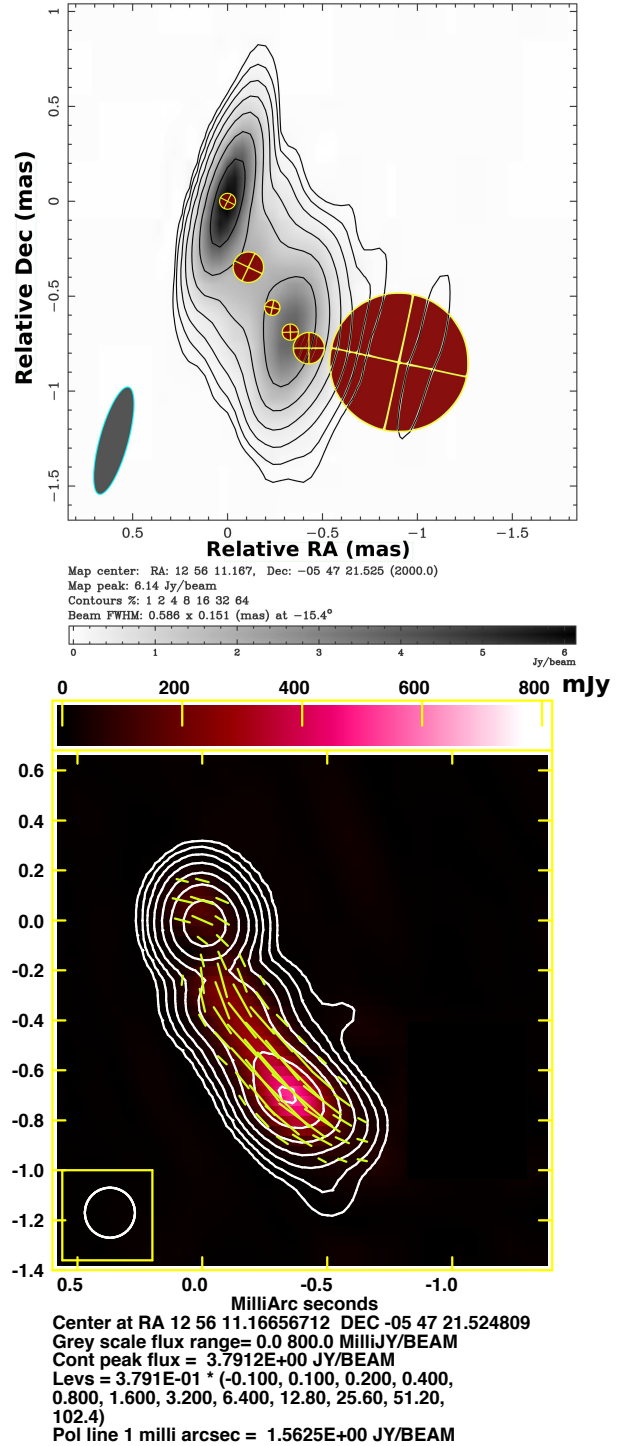


FIG. 11.— Top: An example image of 3C 279 as observed in February 2014: Gaussian circular components plotted on top of the total intensity contours. Bottom: Composite total (contours) and polarized (color) intensity image of 3C 279 convolved with a beam size of 0.1 mas. The line segments (length of the segments is proportional to fractional polarization) show the EVPA direction. The ellipse/circle in the bottom left corner is the synthesized beam of the array.

#### 3.3.1. Component motion

The VLBI core centered at (RA 12 56 11.167 DEC -05 47 21.53) is chosen as a reference point, and is fixed to coordinates (0, 0) to study the kinematics of individual components. The absolute position of the core could change because

TABLE 1  
KINEMATICAL PARAMETERS OF THE JET EMISSION

Component	$\mu$ (mas yr <sup>-1</sup> )	$\beta_{app}$ (c)	$T_0$ (days)
C1	0.49 ± 0.04	15.8 ± 1.2	–
C2	0.58 ± 0.03	18.4 ± 0.8	–
C3	0.69 ± 0.02	21.8 ± 0.7	–
NC1	0.71 ± 0.02	22.4 ± 0.7	1558 <sup>-28</sup> <sub>+15</sub>
NC2	0.55 ± 0.03	17.5 ± 0.8	1638 <sup>-27</sup> <sub>+40</sub>
NC3	0.61 ± 0.04	19.2 ± 1.2	1810 <sup>-19</sup> <sub>+26</sub>

$\mu$  : angular speed  
 $\beta_{app}$  : apparent velocity  
 $T_0$  : component's core separation time

of changes in opacity, pressure or instabilities in the jet (see Hodgson et al. 2017; Lisakov et al. 2017, for details). However either we fix the core position to (0,0) or leave it free, it does not affect the relative separation of the components w.r.t. the core. During the course of our campaign period, we identified a total of 6 components - C1, C2, C3, NC1, NC2, and NC3 - in addition to the core. Figure 12 shows the evolution of the radial distance of the components from the core (a) and their trajectories in the XY-plane<sup>12</sup> projected on the sky (b). The flux density variations in the individual knots are shown in Fig. 12 (c).

In August 2013, the jet's brightness could be well described using five components (C1 to C3 and two unidentified components) in addition to the core (see Tab. 2 in Appendix). A new component (NC1) appeared in November 2013, followed by the ejection of two more components in May (NC2) and December (NC3) 2014. The core brightened before the ejection of a new component and later the component appeared in the jet. All these components exhibit significant motion especially in the radial direction. As seen in Fig. 12 (b), the components tend to follow the same linear trajectories in the XY-plane up to a distance of  $\sim 0.5$  mas. This is in contrast to what we usually observe for blazars. Wiggly/curved trajectories of components are often seen for blazars (see Rani et al. 2014, 2015; Chatterjee et al. 2008; Lister et al. 2013, and references therein).

To study the component motion in the radial direction, we fitted the radial separation of the components relative to the core using,  $r(t) = \mu \times (t - T_0)$ , where  $\mu$  is the angular speed in mas yr<sup>-1</sup> and  $T_0$  corresponds to the ejection time of the components from the core. The solid lines in Fig. 12 (a) represent the best-fitted functions. The fit provides the angular speed ( $\mu$ ), which we used to calculate the apparent velocity following  $\beta_{app} = \frac{\mu \cdot D_L}{c \cdot (1+z)}$ , where  $D_L$  is the luminosity distance and  $z$  is the redshift of the source. In Table 1, we list the angular and apparent speeds of the components. Back-extrapolation of the components' motion is used to estimate the ejection time of the new components (NC1 to NC3). The calculated ejection times of the new components are listed in Table 1. The highest detected apparent speed ( $\beta_{app}$ ) can be used to get an estimate on the lowest possible Lorentz factor,  $\Gamma \geq (1 + \beta_{app}^2)^{0.5}$  and maximum viewing angle,  $\theta_{view} \leq \sin^{-1}(1/\beta_{app})$ . Using  $\beta_{app} = 22.4$ , we get  $\Gamma \geq 22.4$  and  $\theta_{view} \leq 2.6^\circ$ .

### 3.4. Polarization variations

<sup>12</sup>  $X = r \cos(\theta + 90^\circ)$  and  $Y = r \sin(\theta + 90^\circ)$ ;  $r$  is the radial separation from the core and  $\theta$  is the position angle with respect to an imaginary north-south line drawn through the map center

Figure 13 presents a comparison of the variations observed in percentage polarization (PP) at optical and radio frequencies (left y-scale is for the optical data while the right is for the radio data). Although it is difficult to make a one-to-one comparison between the PP variations at the two frequencies because of sparse sampling of the radio data but we do see a similarity. For instance, in the beginning the PP is high both at optical and radio bands. A drop in PP (between JD' 1600 and 1680) is observed almost simultaneously at the two frequencies. An increase in PP appears after the dip observed in optical and 230 GHz data but not in the 43 GHz VLBI data. PP in the core region remains rather constant after the dip. On the other hand, PP at optical and 230 GHz radio frequencies continue rising until they regain their initial value at the end of the observations.

Figure 13 (bottom) shows a comparison of the EVPA variations at optical and radio frequencies. In contrast to PP, EVPA variations are rather modest. A peak to peak (minimum to maximum) change of  $\sim 60^\circ$  is observed in the optical and 43 GHz VLBI data, and in the 230 GHz data, it is  $\leq 25^\circ$ . The average EVPA values at the three frequencies are also quite similar ( $\sim 40^\circ - 60^\circ$ ). This indicates that the optical and radio polarization angles (EVPAs) are roughly parallel to the jet direction<sup>13</sup> ( $\sim -135^\circ$ ). We noticed a change in the VLBI core EVPA during the ejection of new components (NC2 and NC3), which could be because of a different EVPA orientation of the new component(s).

The PP (top) and EVPA (bottom) variations observed in the new ejected components are shown in Fig. 14. The PP of the components gradually increase after their separation from the core and stay as high as  $\geq 20\%$ . This could result from either a transition from the optically thick to thin regime at 43 GHz or a progressive ordering of the magnetic field with distance down the jet. The EVPAs of the new components (especially NC2) show some modest variations but still remain aligned along the jet axis.

### 3.5. Flux density vs. polarization variations

In Fig. 15, we show a comparison of optical flux density and polarization variations. We used an inverse y-scale for the optical PP data. During the first 3  $\gamma$ -ray flares ("1" to "3"), the optical flux is rising and a decay is seen in the PP. Peaks of flares "4" to "5" coincide with the dips in the PP curve indicating a clear anti-correlation between the two. The anti-correlation is even more evident in the PP vs. optical flux plot on the right. A formal linear Pearson correlation test suggests a significant anti-correlation between the optical flux and polarization data; we obtained  $r_P = -0.76$ , at the  $>99.99999\%$  confidence level.

A comparison of the optical PP and  $\gamma$ -ray photon flux variations is shown in Fig. 16 (left) (again an inverse-scale is used for the optical PP data). There are hints of an apparent anti-correlation between the two. For instance, at the onset of the  $\gamma$ -ray outburst (JD'  $\sim 1610$ ), the optical PP is quite high ( $\sim 25\%$ ). Also, the peaks of  $\gamma$ -ray flares ("4" and "5") roughly coincide with the dips in the PP curve. Finally, the optical PP regained its original value ( $\sim 25\%$ ) at the end of the outburst (JD'  $\sim 1820$ ). The anti-correlation is even more evident in the optical PP vs.  $\gamma$ -ray photon flux plot shown in the right panel of Fig. 16. The statistical significance is tested via the linear-Pearson correlation analysis, which suggests a significant ( $r_P$

<sup>13</sup> Since at optical frequencies, we are already in the optically thin regime, the Faraday effects are negligible here.

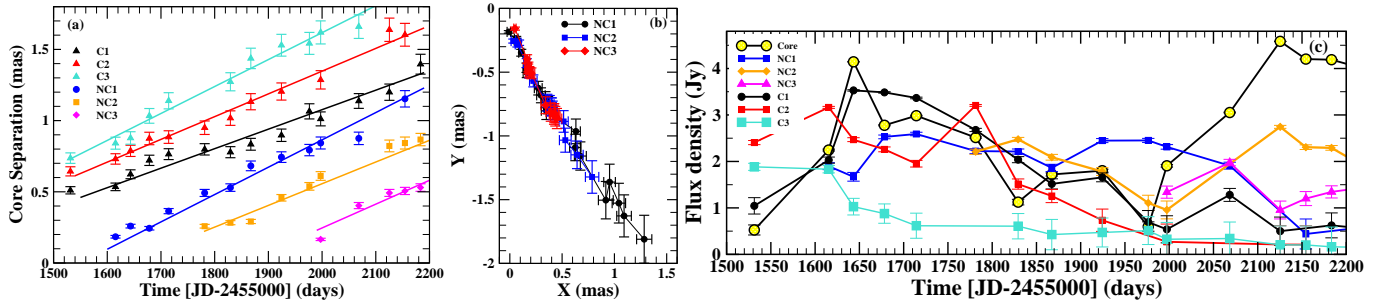


FIG. 12.— (a) Temporal evolution of the components' radial separation from the core; the solid lines represent fits with a linear function. (b) Trajectories of the components in the X-Y plane (see Section 3.3.1 for details). (c) Flux density variations of the individual knots.

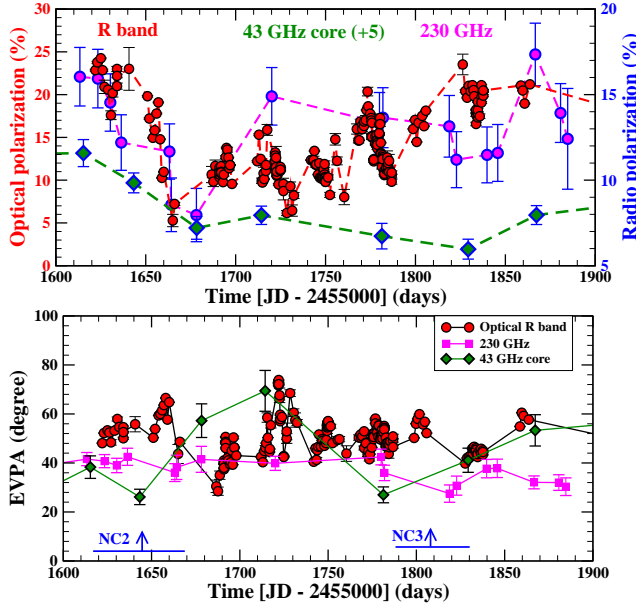


FIG. 13.— *Top*: A comparison of the percentage polarization variations at radio and optical frequencies. For illustration purposes, the 43 GHz radio core percentage polarization curve is shifted by +5 Jy (left scale should be used for the optical data and right for the radio data). EVPA variations are displayed in the *bottom* panel.

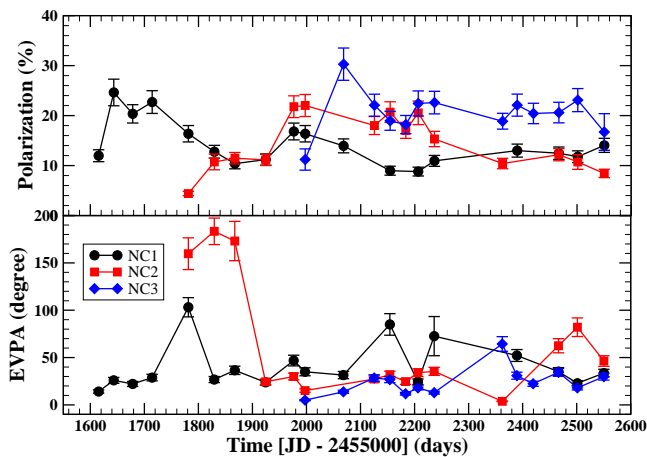


FIG. 14.— Percentage polarization and EVPA variations observed in the individual components.

$= -0.27$  at a confidence level = 98.5%) anti-correlation between the two.

Figure 17 shows the PP vs. spectral index plot. We again used the linear-Pearson correlation analysis to test the significance of the correlation between PP and optical/ $\gamma$ -ray spec-

tral indices. Formally we obtained  $r_P = 0.63$  at the 99.9998% confidence level for the PP vs.  $\gamma$ -ray photon index data (see top panel), which suggests a significant correlation between the two. The PP vs. optical spectral index plot suggests a correlation ( $r_P = 0.57$ ) at the 93.7% confidence level. A positive correlation between PP and optical/ $\gamma$ -ray spectral indices indicates that higher PP is observed for a steeper spectrum. A significant hardening of the optical/ $\gamma$ -ray spectrum is observed during bright flares (see Section 3.1.1 and 3.1.3 for details).

Change in PP could be simply explained either by a change in B-field order (i.e. an increase in PP indicates a more ordered magnetic field) or by a change in the spectral index of the emitting particles. We could expect to see some increase in PP due to steepening of the electron spectrum or the synchrotron spectrum (degree of maximum polarization =  $(\alpha + 1)/(\alpha + 5/3)$ , where  $\alpha$  is the spectral index). For instance, steepening of a spectrum by one magnitude ( $\Delta\alpha = 1$ ) produces a  $\leq 5\%$  increment in PP magnitude. Although the PP significantly correlates with  $\alpha$ , our observations suggest variations of 20% ( $\Delta PP = 20$ ). This in turn suggests that the PP variations cannot be solely explained via steepening of the spectrum as a change in the spectral index has only a very slight affect on the PP.

Since the mean polarization is the maximum divided by the square-root of the number of cells<sup>14</sup> involved in the emission, the observed anti-correlation between gamma-ray flux and optical PP could be because of the presence of more turbulent cells during the outburst than at other times. The jet plasma is highly dynamic; plasma instabilities (e.g., the current-driven kink instability and/or magnetohydrodynamical instabilities Nishikawa et al. 2016; Nalewajko & Begelman 2012) could occur and vary with time, which basically drives the turbulence. In short, instabilities drive turbulence which can influence the number of cells in a given emission region. This in turn implies that the turbulence could enhance the efficiency of particle acceleration, which is why there is an outburst and also why the spectrum is flatter during the outburst and steeper before and after the outburst when the PP is higher. An observational test of the turbulence cell model (TEMZ, Marscher 2014) is to compare the standard deviation of random PP fluctuations (compared to the systematic variations). In case of the presence of only turbulent component(s)  $\sigma(PP) = 0.5 \langle PP \rangle$ . We used equal time bin when the PP is not changing systematically to determine  $\sigma(PP)$ . For 3C 279 the calculated  $\sigma(PP) = (0.08 \text{ to } 0.25) \langle PP \rangle$ , which suggests the presence of a polarized steady component as well as the presence of multiple emission components with different polar-

<sup>14</sup> the smallest scale emission region having a preferred magnetic field orientation (Marscher 2014)

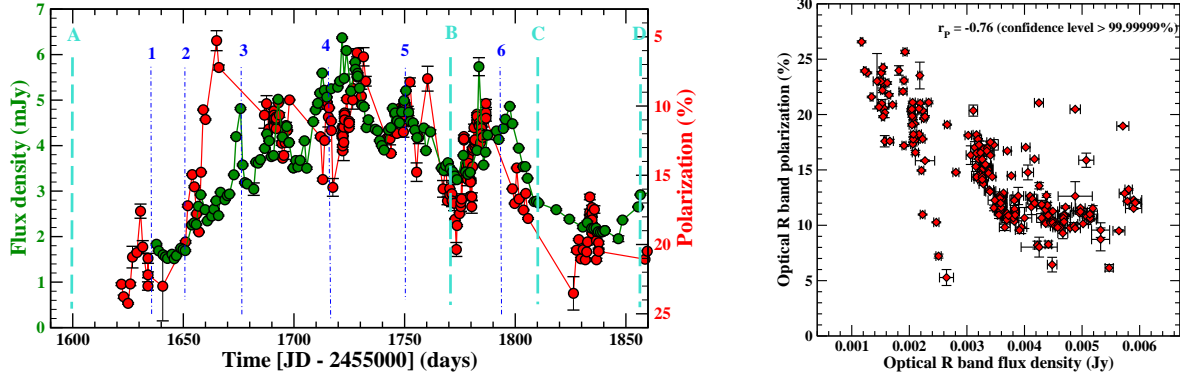


FIG. 15.— *Left*: Optical R band flux density variations superimposed with the optical percentage polarization variations (vertical dotted and dashed lines are same as in Fig. 1). The right y-scale is for optical polarization, and is reversed for comparison purposes. *Right*: Optical polarization vs. flux density plot.

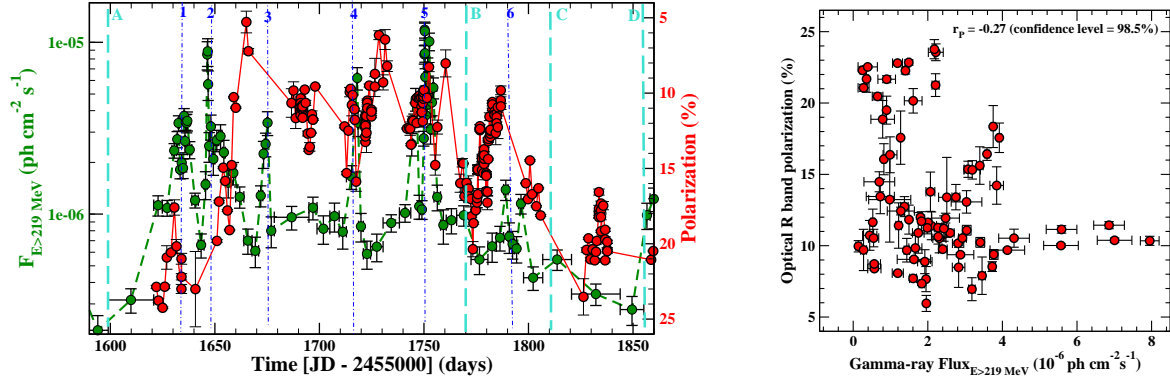


FIG. 16.— *Left*: Gamma-ray photon flux variations superimposed on the optical percentage polarization variations (vertical dotted and dashed lines are same as in Fig. 1). The right y-scale is for optical polarization, and is reversed for comparison purposes. *Right*: Optical polarization vs.  $\gamma$ -ray photon flux plot.

izations.

To further test the hypothesis of the presence of a steady polarized component in addition to the multiple turbulent components, we investigate the variations in Stokes Q and U parameters. Photometric and polarimetric measurements obtained on the same day were used to calculate the fractional Stokes parameters,  $Q_{frac} = PP \cos(2 \times EVPA)$  and  $U_{frac} = PP \sin(2 \times EVPA)$ . Figure 18 (left) shows the variations in optical R band  $Q_{frac}$  and  $U_{frac}$ . A clear difference in the Stokes  $Q_{frac}$  and  $U_{frac}$  variations can be noticed here. The observed dependence between the Stokes parameters is given in the right panel of Fig. 18 (red: optical R band, magenta: 43 GHz radio core, blue: 230 GHz, and green: 86 GHz). The  $Q_{frac}, U_{frac}$  centroid clearly deviates from (0,0). We noticed similar shift at 86 and 230 GHz radio bands, and also in the 43 GHz radio core. The observed shift of the Q,U centroid with respect to (0,0) can be explained by the presence of a steady components with polarization direction aligned along the jet axis (Blinov & Hagen-Thorn 2009). Moreover, a similarity of EVPA values at optical and radio frequencies with the VLBI core EVPAs supports the alignment of optical/radio polarization direction along the jet axis (Section 3.4). As is suggested by Blinov & Hagen-Thorn (2009), if the steady polarized component has a higher degree of polarization, one can expect to see an anti-correlation between the flux and degree of polarization. The observed PP at the beginning/end of the outburst (see Figs. 15 and 16) is  $\sim 25\%$ , which means that the steady polarized component is higher than 25%. A steady polarized component having its direction parallel to the jet axis could be the toroidal magnetic field component of the jet. Alternatively, the presence of multiple emission components

with different polarizations could be plausible as well.

### 3.6. Connection between jet activity and broadband emission

Given the superposition of multiple modes of flaring activity, it is quite challenging to understand the broadband flaring behavior of the source. The major outburst (A to D) is accompanied by faster flares across the whole electromagnetic spectrum (see Fig. 1). Interestingly, a new component “NC2” is ejected from the core during the period of the first three (“1” to “3”)  $\gamma$ -ray flares. The next three flares (“4” to “6”) were followed by a continuous decay in the source brightness at  $\gamma$ -ray, optical, and radio frequencies between period “C” and “D”. Later, the ejection of a new component “NC3” from the core suggests a delay between the high-energy activity and the component’s core-separation timing.

Simulations (as described in Appendix A) were used to test whether the connection between component ejection and  $\gamma$ -ray flaring activity is just by chance or not. First we simulated a total of 1000 light curves. Next, we checked how often do we see a gamma-ray flare in the simulated data during the ejection of NC2 (JD’ = 1611 to 1678) and NC3 (JD’ = 1790 to 1836). Given the superposition of multiple modes of flaring activity, defining a flare could be tricky. We choose a simplistic approach here. As the typical duration of the rapid  $\gamma$ -ray flares (1 to 6) is 10 to 30 days, we define a continuous rise in the  $\gamma$ -ray flux above  $6.6 \times 10^{-7}$  ph cm $^{-2}$  s $^{-1}$  (two times above the quiescent level) for  $\geq 20$  days as a flare, and tested how often this condition is met in our simulated light curves. During the NC2 ejection period, we found a flare in 28 out of 1000 cases; in short, the ejection of NC2 is connected to the  $\gamma$ -ray flaring activity with 97.2% confidence level. Similar, we

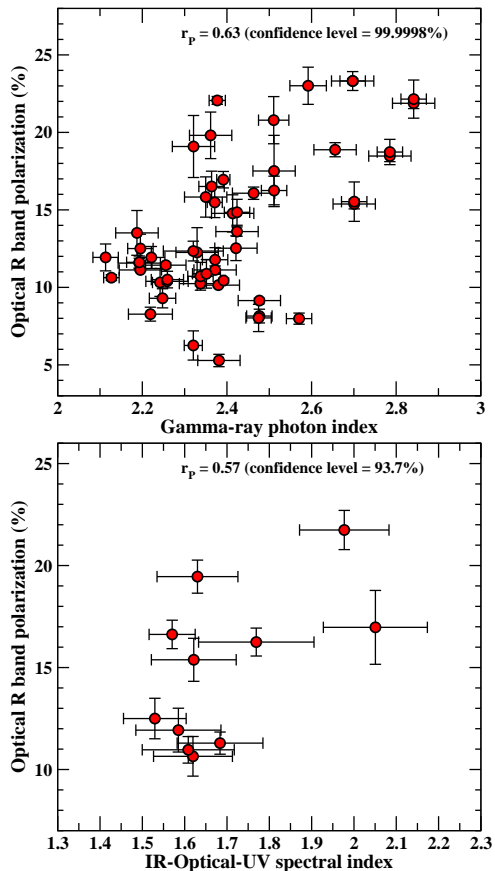


FIG. 17.— Optical polarization vs.  $\gamma$ -ray photon index (*top*) and IR-optical-UV spectral index (*bottom*).

found that the  $\gamma$ -ray flares are related to NC3 with a 95.8% confidence level. We also tested the significance of connection between  $\gamma$ -ray flares observed within 50 days before and after the ejection of the components. Our calculations suggest that the chance-coincidence of NC2 being associated to a flare(s) 50 days before or after its ejection is below 90%. In case of NC3, there are fair chances (94.2%) that its ejection could be related to a flare(s) observed 50 days prior to the ejection, while the confidence-level of its ejection being connected to a flare observed with 50 days after to its ejection is below 90%. Moreover, we tested the chance-coincidence for the different flare durations. For a short flare duration of 10 days, the probability of observing a flare by chance during the ejection of NC2 (and NC3) is less than 10% i.e. the confidence level of NC2 (and NC3) being associated with a  $\gamma$ -ray flare is  $\simeq 90\%$ . In case of a long-duration flare (30 days), the confidence level is  $>96\%$ .

### 3.7. Multiple energy dissipation regions

During 2013-2014, we observed two modes of flaring activity (faster flares sitting on top of the long-term outburst) in 3C 279 at radio, optical and  $\gamma$ -ray energies. Although X-ray counterparts were observed for two flares, the long-term outburst seems to be missing. The broadband SED modeling during this period (reported in Hayashida et al. 2015) suggests that single zone emission models that matched the optical and  $\gamma$ -ray spectra failed to describe the X-ray emission, which suggests the presence of multiple emission regions.

Unlike the last three flares (“4” to “6”), the first three  $\gamma$ -ray flares (“1” to “3”) are missing their optical/radio counterparts,

except for flare “3” which is observed at optical bands. Moreover, the IOU spectrum is relatively softer ( $\alpha_{IOU} \sim 1.8-2.0$ ) during the first episode of flares. Later, the IOU spectrum gets harder ( $\alpha_{IOU} \sim 1.6$ ). A new component, NC2, appeared in the jet during the flare “1” to “3”. Ejection of NC2 during the first three flares indicates that these high-energy flares have to be produced either at the VLBI core or very close to the core region; otherwise, we would have observed a delay between the high-energy flares and the component ejection, which we did not. A delay is observed between the last three flares (4 to 6) and the ejection of NC3. This indicates that the high-energy region is located further upstream of the VLBI core (closer to the central BH). Moreover, the PP vs.  $\gamma$ -ray/optical flux and spectral index correlation (discussed in Section 3.5) suggests the presence of multiple turbulent cells in a given emission region and also that the number of these cells is variable with time.

We interpret the observed broadband flaring activity in the following manner (see Fig. 19). A disturbance at the base of the jet could cause a shock wave and propagate down the jet, and could be related to the onset of the major outburst (Fig. 19 a). Later, the moving shock reaches the 43 GHz core producing the first 3 flares (1 to 3). Given the different B-field properties of cells, the particle acceleration efficiency could be different for different cells. Since at a given frequency, what we observe is their collective emission, concurrent broadband flaring activity may or may not be observed. The moving shock disturbs the jet outflow and becomes knot NC2 as it separates from the core (Fig. 19 b). In the second episode of flaring activity (4 to 5), the emission region seems to be located further upstream of the core (closer to the central black hole, see: Fig. 19 c). Later, the disturbance/shock wave passes the core region resulting in the ejection of NC3 (Fig. 19 d). Our analysis therefore supports two possible energy dissipation sites in 3C 279. Location of the dissipation zone depends on the parameters of a disturbance, especially the Lorentz factor ( $\Gamma$ ), and for disturbances with lower  $\Gamma$  the dissipation zone is expected to be closer to the BH than for those with larger  $\Gamma$  (Katarzyński & Ghisellini 2007). Although  $\beta_{app}$  of NC2 and NC3 are similar within the uncertainties, it is possible that  $\Gamma_{NC2} > \Gamma_{NC3}$  that would result in the dissipation zone during the flares 1-3 to be farther from the BH and closer to the VLBI core. Both observations (Rani et al. 2015; Hodgson et al. 2017; Jorstad et al. 2005) and simulations (Gómez et al. 1997; Fromm et al. 2012) support the presence of standing shocks in parsec-scale AGN jets. In fact at short mm-radio bands, the VLBI core could be a standing shock as well (Hodgson et al. 2017; Marscher 2008). Passage of a moving shock through standing shocks is quite efficient in accelerating particles to high energies, which could explain why some sites are more favored than others for energy dissipation (Gómez et al. 1997; Meyer et al. 2015).

## 4. SUMMARY AND CONCLUSION

We used high-frequency VLBI observations to probe the broadband flaring activity in 3C 279. At GeV energies the source went through a series of flares superimposed on a long-term outburst from  $JD' = 1600$  to 1850 (November 2013 to August 2014). In total we observed 6  $\gamma$ -ray flares, and four of these flares have optical (and radio) counterparts. X-ray counterparts are only observed for two flares (2 and 5). Moreover, similar to  $\gamma$  rays, we observed two different modes of flaring activity (fast flares superimposed on a long-term outburst) at optical and radio frequencies. On the other hand, the

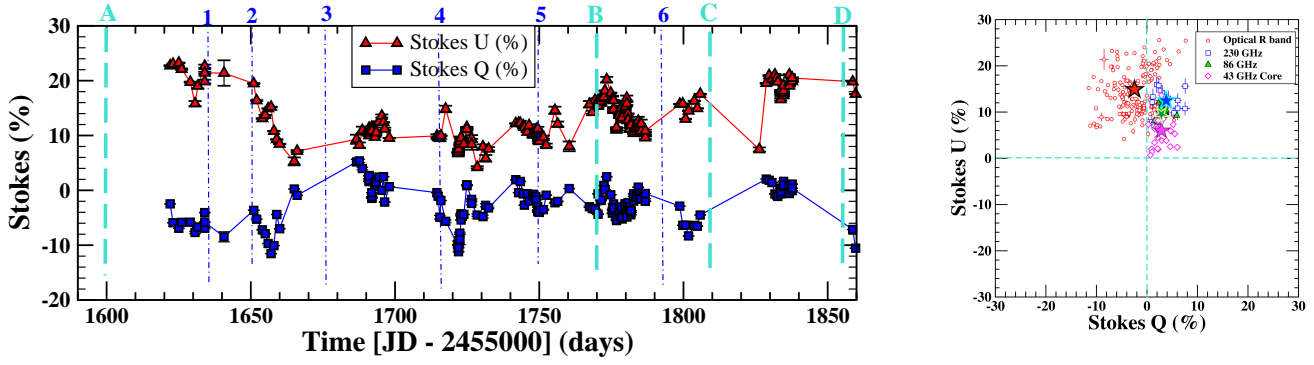


FIG. 18.— *Left*: Optical R band  $Q_{frac}$  and  $U_{frac}$  variations (vertical dotted and dashed lines are same as in Fig. 1). *Right*: Stokes  $Q_{frac}$  versus  $U_{frac}$ ; centroid in each case is marked with a star.

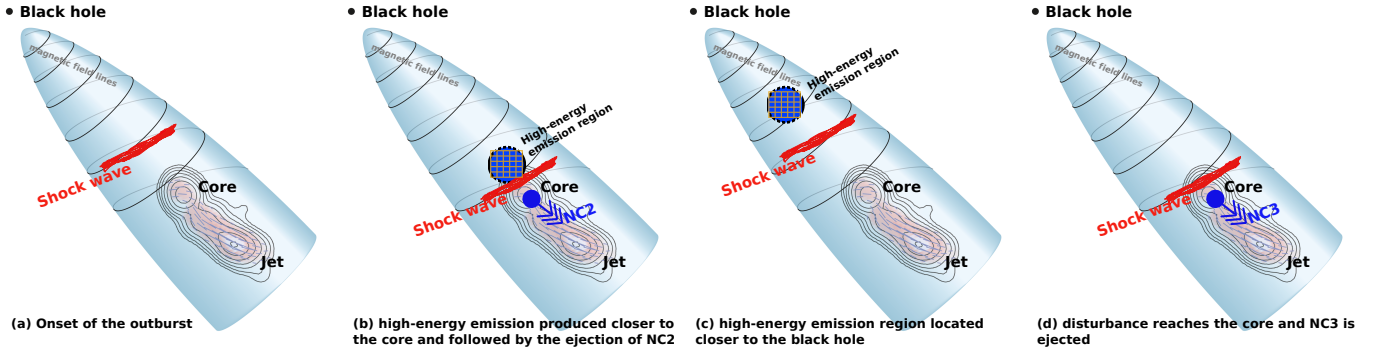


FIG. 19.— Sketch for the proposed scenario in the 3C 279 (not to scale): a disturbance (or shock wave) reaches the core (a) producing the high-energy flares (“1” to “3”) closer to the core region and an ejection of component NC2 (b). (c) High-energy emission region is located closer to the black hole, and later, the disturbance passes the core resulting into the ejection of NC3 (d).

long-term outburst activity seems to be missing at X-rays.

Two modes (fast flares superimposed on long-term variations) of variability are also observed in percentage polarization (PP) data at optical and radio frequencies. On the other hand, the polarization angle (EVPA) variations are quite modest at both optical and radio frequencies, and the EVPAs are well aligned with the jet direction.

Two new components (NC2 and NC3) were ejected from the core during the flaring activity period, and are connected to the source flaring activity with  $\geq 95\%$  probability. NC2 appeared in the jet during the first three flares (1 to 3) pointing to the the 43 GHz VLBI core as the possible location of energy dissipation. Ejection of NC3 happened after the last three flares (4 to 6), which puts the location of energy dissipation further upstream of the VLBI core (in a region closer to the BH). Our analysis therefore argues in favor of multiple energy dissipation regions in the source.

We detected an anti-correlation between the optical PP and  $\gamma$ -ray/optical flux variations, while, a positive correlation is seen for the PP and  $\gamma$ -ray/optical spectral index variations. We propose that this could be explained using the turbulent multi-zone cell model (TEMZ). If there are more turbulent cells in the emission region during the outburst than other times, one might expect to see an anti-correlation between  $\gamma$ -ray/optical flux and PP. This in turn implies that the turbulence is related to the efficiency of particle acceleration. The observations however solely cannot be described using the turbulent component. A shift in Stokes (Q,U) centroid w.r.t. (0,0) suggests the presence of multiple emission components with different polarizations.

The *Fermi*/LAT Collaboration acknowledges generous ongoing support from a number of agencies and institutes that have supported both the development and the operation of the LAT as well as scientific data analysis. These include the National Aeronautics and Space Administration and the Department of Energy in the United States, the Commissariat à l’Energie Atomique and the Centre National de la Recherche Scientifique / Institut National de Physique Nucléaire et de Physique des Particules in France, the Agenzia Spaziale Italiana and the Istituto Nazionale di Fisica Nucleare in Italy, the Ministry of Education, Culture, Sports, Science and Technology (MEXT), High Energy Accelerator Research Organization (KEK) and Japan Aerospace Exploration Agency (JAXA) in Japan, and the K. A. Wallenberg Foundation, the Swedish Research Council and the Swedish National Space Board in Sweden. Additional support for science analysis during the operations phase is gratefully acknowledged from the Istituto Nazionale di Astrofisica in Italy and the Centre National d’Études Spatiales in France. This work performed in part under DOE Contract DE-AC02-76SF00515.

This research was supported by an appointment to the NASA Postdoctoral Program at the Goddard Space Flight Center, administered by Universities Space Research Association through a contract with NASA. This study makes use of 43 GHz VLBA data from the VLBA-BU Blazar Monitoring Program (VLBA-BU-BLAZAR; <http://www.bu.edu/blazars/VLBAproject.html>), funded by NASA through the Fermi Guest Investigator Program. The VLBA is an instrument of the Long Baseline Observatory. The Long Baseline Observatory is a facility of the National Science Foundation operated by Associated Universities, Inc. The BU group acknowledges support from US National Sci-

ence Foundation grant AST-1615796. The Submillimeter Array is a joint project between the Smithsonian Astrophysical Observatory and the Academia Sinica Institute of Astronomy and Astrophysics and is funded by the Smithsonian Institution and the Academia Sinica. This research was supported by an appointment to the NASA Postdoctoral Program at the Goddard Space Flight Center, administered by Universities Space Research Association through a contract with NASA. KS is supported by the Russian Science Foundation grant 16-12-10481. The St. Petersburg University team acknowledges support from Russian Science Foundation grant 17-12-01029. This research has made use of data from the OVRO 40-m monitoring program (Richards et al. 2011) which is supported

in part by NASA grants NNX08AW31G, NNX11A043G, and NNX14AQ89G and NSF grants AST-0808050 and AST-1109911. IA acknowledges support by a Ramón y Cajal grant of the Ministerio de Economía, Industria, y Competitividad (MINECO) of Spain. Acquisition and reduction of the POLAMI data was supported in part by MINECO through grants AYA2010-14844, AYA2013-40825-P, and AYA2016-80889-P, and by the Regional Government of Andalucía through grant P09-FQM-4784. The POLAMI observations were carried out at the IRAM 30m Telescope. IRAM is supported by INSU/CNRS (France), MPG (Germany) and IGN (Spain). BR acknowledges the help of Roopesh Ojha, Marcello Giroletti, and Dave Thompson for fruitful discussions and comments that improved the manuscript.

## REFERENCES

- Abdo, A. A., Ackermann, M., Agudo, I., et al. 2010, *ApJ*, 716, 30  
 Acero, F., Ackermann, M., Ajello, M., et al. 2015, *ApJS*, 218, 23  
 Ackermann, M., Anantua, R., Asano, K., et al. 2016, *ApJ*, 824, L20  
 Agudo, I., Thum, C., Gómez, J. L., & Wiesemeyer, H. 2014, *A&A*, 566, A59  
 Agudo, I., Thum, C., Ramakrishnan, V., et al. 2018a, *MNRAS*, 473, 1850  
 Agudo, I., Thum, C., Wiesemeyer, H., & Krichbaum, T. P. 2010, *ApJS*, 189, 1  
 Agudo, I., Marscher, A. P., Jorstad, S. G., et al. 2011, *ApJ*, 735, L10  
 Agudo, I., Thum, C., Molina, S. N., et al. 2018b, *MNRAS*, 474, 1427  
 Albert, J., Aliu, E., Anderhub, H., et al. 2008, *Science*, 320, 1752  
 Atwood, W. B., Abdo, A. A., Ackermann, M., et al. 2009, *ApJ*, 697, 1071  
 Blinov, D. A., & Hagen-Thorn, V. A. 2009, *A&A*, 503, 103  
 Bonning, E., Urry, C. M., Bailyn, C., et al. 2012, *ApJ*, 756, 13  
 Böttcher, M., Basu, S., Joshi, M., et al. 2007, *ApJ*, 670, 968  
 Burbidge, E. M., & Rosenberg, F. D. 1965, *ApJ*, 142, 1673  
 Burrows, D. N., Hill, J. E., Nousek, J. A., et al. 2005, *Space Sci. Rev.*, 120, 165  
 Chatterjee, R., Jorstad, S. G., Marscher, A. P., et al. 2008, *ApJ*, 689, 79  
 Cheung, C. C. 2002, *ApJ*, 581, L15  
 Chidiac, C., Rani, B., Krichbaum, T. P., et al. 2016, *A&A*, 590, A61  
 Collmar, W., Böttcher, M., Krichbaum, T. P., et al. 2010, *A&A*, 522, A66  
 Connolly, S. 2015, *ArXiv e-prints*, arXiv:1503.06676  
 Cutini, S. 2015, *The Astronomer's Telegram*, 7633, 1  
 Emmanoulopoulos, D., McHardy, I. M., & Papadakis, I. E. 2013, *MNRAS*, 433, 907  
 Fromm, C. M., Perucho, M., Ros, E., et al. 2012, *International Journal of Modern Physics Conference Series*, 8, 323  
 Gómez, J. L., Martí, J. M., Marscher, A. P., Ibáñez, J. M., & Alberdi, A. 1997, *ApJ*, 482, L33  
 Gu, M., Cao, X., & Jiang, D. R. 2001, *MNRAS*, 327, 1111  
 Gurwell, M. A., Peck, A. B., Hostler, S. R., Darrah, M. R., & Katz, C. A. 2007, in *Astronomical Society of the Pacific Conference Series*, Vol. 375, From Z-Machines to ALMA: (Sub)Millimeter Spectroscopy of Galaxies, ed. A. J. Baker, J. Glenn, A. I. Harris, J. G. Mangum, & M. S. Yun, 234  
 Hartman, R. C., Bertsch, D. L., Fichtel, C. E., et al. 1992, *ApJ*, 385, L1  
 Hartman, R. C., Webb, J. R., Marscher, A. P., et al. 1996, *ApJ*, 461, 698  
 Hayashida, M., Madejski, G. M., Nalewajko, K., et al. 2012, *ApJ*, 754, 114  
 Hayashida, M., Nalewajko, K., Madejski, G. M., et al. 2015, *ApJ*, 807, 79  
 Hodgson, J. A., Krichbaum, T. P., Marscher, A. P., et al. 2017, *A&A*, 597, A80  
 Homan, D. C., Lister, M. L., Aller, H. D., Aller, M. F., & Wardle, J. F. C. 2009, *ApJ*, 696, 328  
 Jorstad, S., & Marscher, A. 2016, *Galaxies*, 4, 47  
 Jorstad, S. G., Marscher, A. P., Lister, M. L., et al. 2004, *AJ*, 127, 3115  
 —. 2005, *AJ*, 130, 1418  
 Jorstad, S. G., Marscher, A. P., Larionov, V. M., et al. 2010, *ApJ*, 715, 362  
 Jorstad, S. G., Marscher, A. P., Morozova, D. A., et al. 2017, *ApJ*, 846, 98  
 Kalberla, P. M. W., Burton, W. B., Hartmann, D., et al. 2005, *A&A*, 440, 775  
 Kang, S., Lee, S.-S., & Byun, D.-Y. 2015, *Journal of Korean Astronomical Society*, 48, 257  
 Katarzyński, K., & Ghisellini, G. 2007, *A&A*, 463, 529  
 Larionov, V. M., Jorstad, S. G., Marscher, A. P., et al. 2008, *A&A*, 492, 389  
 Lisakov, M. M., Kovalev, Y. Y., Savolainen, T., Hovatta, T., & Kutkin, A. M. 2017, *MNRAS*, 468, 4478  
 Lister, M. L., Aller, M. F., Aller, H. D., et al. 2013, *ArXiv e-prints*, arXiv:1308.2713  
 Lott, B., Escande, L., Larsson, S., & Ballet, J. 2012, *A&A*, 544, A6  
 Maraschi, L., Grandi, P., Urry, C. M., et al. 1994, *ApJ*, 435, L91  
 Marscher, A. P. 2008, in *Astronomical Society of the Pacific Conference Series*, Vol. 386, Extragalactic Jets: Theory and Observation from Radio to Gamma Ray, ed. T. A. Rector & D. S. De Young, 437  
 Marscher, A. P. 2014, *ApJ*, 780, 87  
 Mattox, J. R., Bertsch, D. L., Chiang, J., et al. 1996, *ApJ*, 461, 396  
 Mead, A. R. G., Ballard, K. R., Brand, P. W. J. L., et al. 1990, *A&AS*, 83, 183  
 Meyer, E. T., Georganopoulos, M., Sparks, W. B., et al. 2015, *Nature*, 521, 495  
 Nalewajko, K., & Begelman, M. C. 2012, *MNRAS*, 427, 2480  
 Nishikawa, K.-I., Mizuno, Y., Niemi, J., et al. 2016, *Galaxies*, 4, 38  
 Poole, T. S., Breeveld, A. A., Page, M. J., et al. 2008, *MNRAS*, 383, 627  
 Rani, B., Krichbaum, T. P., Hodgson, J. A., & Zensus, J. A. 2016, *ArXiv e-prints*, arXiv:1601.04693  
 Rani, B., Krichbaum, T. P., Lee, S.-S., et al. 2017, *MNRAS*, 464, 418  
 Rani, B., Krichbaum, T. P., Marscher, A. P., et al. 2015, *A&A*, 578, A123  
 —. 2014, *A&A*, 571, L2  
 Richards, J. L., Max-Moerbeck, W., Pavlidou, V., et al. 2011, *ApJS*, 194, 29  
 Roming, P. W. A., Kennedy, T. E., Mason, K. O., et al. 2005, *Space Sci. Rev.*, 120, 95  
 Schlegel, D. J., Finkbeiner, D. P., & Davis, M. 1998, *ApJ*, 500, 525  
 Smith, P. 2016, *Galaxies*, 4, 27  
 Spergel, D. N., Verde, L., Peiris, H. V., et al. 2003, *ApJS*, 148, 175  
 Taylor, G. B. 2000, *ApJ*, 533, 95  
 Thum, C., Agudo, I., Molina, S. N., et al. 2018, *MNRAS*, 473, 2506  
 Thum, C., Wiesemeyer, H., Paubert, G., Navarro, S., & Morris, D. 2008, *PASP*, 120, 777  
 Vaughan, S., Edelson, R., Warwick, R. S., & Uttley, P. 2003, *MNRAS*, 345, 1271  
 Wagner, S. J., & Mannheim, K. 2001, in *Astronomical Society of the Pacific Conference Series*, Vol. 250, Particles and Fields in Radio Galaxies Conference, ed. R. A. Laing & K. M. Blundell, 142  
 Wardle, J. F. C., Homan, D. C., Ojha, R., & Roberts, D. H. 1998, *Nature*, 395, 457  
 Wehrle, A. E., Pian, E., Urry, C. M., et al. 1998, *ApJ*, 497, 178  
 Woo, J.-H., & Urry, C. M. 2002, *ApJ*, 579, 530

## APPENDIX

TESTING THE SIGNIFICANCE OF COMPONENT EJECTIONS AND  $\gamma$ -RAY FLARES

The burst-like  $\gamma$ -ray flares in 3C 279 do not follow a Gaussian distribution and can be better described via log-normal or gamma distribution; therefore, we simulated the light curves using the Emmanoulopoulos (Emmanoulopoulos et al. 2013) method implemented by Connolly (2015). The first step is to determine the power spectral density (PSD) slope of the observed  $\gamma$ -ray light curve. Given that the adaptive binned  $\gamma$ -ray data is unevenly sampled, we interpolated it using the cubic spline method in

R<sup>15</sup>. As the data is manipulated via interpolation, we tested our PSD result using simulations. We refer to Chidiac et al. (2016) for a step-by-step analysis. We found that the observed source variability can be well described by a PSD slope of  $-(0.97 \pm 0.17)$ . The method also takes into account of the underlying probability density function (PDF) of the given light curve. We simulated a total of 1000 light curves using the best-fit PDF and PSD parameters. The simulated light curves are sampled at the same cadence as the adaptive binned  $\gamma$ -ray light curve. The average flux and the standard deviation of simulated data is equal to that of the observed data.

#### MODEL FIT COMPONENT RESULTS

Table 2 lists the model fit parameters of the 3C 279 jet. The jet kinematic study is presented in Section 3.3.

<sup>15</sup> <https://stat.ethz.ch/R-manual/R-devel/library/stats/html/splinefun.html>

TABLE 2  
RESULTS FROM GAUSSIAN MODEL FITTING AND COMPONENT PARAMETERS

Epoch (JD')	S	r	$\theta$	$\phi$	Comp <sup>a</sup>
date	(Jy)	(mas)	( $^{\circ}$ )	(mas)	
1531	4.52±0.45	0±0	0±0	0.054±0.005	core
(Aug. 2013)	0.52±0.05	0.28±0.02	-173±17	0.092±0.009	X
	1.04±0.10	0.51±0.05	-160±16	0.074±0.007	C1
	2.40±0.34	0.64±0.06	-155±18	0.087±0.008	C2
	1.88±0.18	0.73±0.07	-153±15	0.154±0.015	C3
	0.38±0.03	1.13±0.11	-128±17	0.693±0.069	X
1615	6.24±0.62	0±0	0±0	0.043±0.004	core
(Nov. 2013)	1.89±0.18	0.18±0.01	177±17	0.109±0.010	NC1
	2.02±0.30	0.53±0.05	-159±15	0.136±0.013	C1
	3.16±0.31	0.73±0.07	-156±20	0.114±0.011	C2
	1.83±0.18	0.84±0.08	-152±15	0.164±0.016	C3
	0.90±0.13	1.03±0.10	-137±22	0.753±0.075	X
1643	8.14±0.81	0±0	0±0	0.062±0.006	core
(Dec. 2013)	1.66±0.16	0.25±0.02	-166±16	0.165±0.016	NC1
	3.52±0.35	0.62±0.06	-156±15	0.136±0.013	C1
	2.46±0.24	0.78±0.07	-154±18	0.078±0.007	C2
	1.02±0.10	0.87±0.08	-150±15	0.134±0.013	C3
	0.55±0.08	1.08±0.10	-132±11	0.653±0.065	X
1678	6.77±0.67	0±0	0±0	0.077±0.007	core
(Jan. 2014)	2.52±0.25	0.24±0.02	-165±16	0.172±0.017	NC1
	1.60±0.16	0.53±0.05	-158±15	0.083±0.008	X
	3.48±0.34	0.72±0.07	-155±15	0.094±0.009	C1
	2.25±0.22	0.87±0.08	-152±15	0.165±0.016	C2
	0.87±0.08	1.03±0.10	-137±13	0.672±0.067	C3
1714	6.98±0.69	0±0	0±0	0.082±0.008	core
(Feb. 2014)	2.59±0.25	0.36±0.03	-162±16	0.164±0.016	NC1
	1.65±0.16	0.60±0.06	-157±15	0.085±0.008	X
	3.36±0.33	0.76±0.07	-154±15	0.087±0.008	C1
	1.95±0.19	0.88±0.08	-151±15	0.164±0.016	C2
	0.61±0.06	1.13±0.11	-133±13	0.775±0.077	C3
1781	6.51±0.65	0±0	0±0	0.073±0.007	core
(May 2014)	2.20±0.22	0.25±0.02	-172±17	0.123±0.012	NC2
	2.22±0.22	0.49±0.04	-161±16	0.096±0.009	NC1
	2.67±0.26	0.79±0.07	-154±15	0.115±0.011	C1
	3.20±0.32	0.94±0.09	-151±15	0.243±0.024	C2
	0.24±0.02	1.73±0.17	-148±14	0.242±0.024	X
1829	5.12±0.51	0±0	0±0	0.068±0.006	core
(Jun. 2014)	2.47±0.24	0.28±0.02	-161±16	0.078±0.007	NC2
	2.21±0.22	0.52±0.05	-162±16	0.065±0.006	NC1
	2.03±0.20	0.77±0.07	-153±15	0.144±0.014	C1
	1.51±0.15	1.01±0.10	-151±15	0.176±0.017	C2
	0.60±0.06	1.27±0.12	-135±13	0.716±0.071	C3
1867	5.71±0.57	0±0	0±0	0.076±0.007	core
(Jul. 2014)	2.09±0.20	0.29±0.02	-165±16	0.233±0.023	NC2
	2.11±0.21	0.50±0.05	-162±16	0.046±0.004	X
	1.86±0.23	0.68±0.06	-156±15	0.108±0.010	NC1
	1.51±0.15	0.83±0.08	-149±14	0.114±0.011	C1
	1.25±0.15	1.13±0.11	-152±15	0.257±0.025	C2
	0.42±0.04	1.43±0.14	-129±12	0.733±0.073	C3
1924	5.80±0.58	0±0	0±0	0.056±0.005	core
(Sep. 2014)	1.89±0.18	0.25±0.02	-157±15	0.137±0.013	X
	1.78±0.17	0.52±0.05	-159±19	0.048±0.004	NC2
	2.44±0.24	0.74±0.09	-156±15	0.098±0.009	NC1
	1.65±0.16	0.87±0.08	-148±18	0.176±0.017	C1
	0.73±0.07	1.20±0.12	-151±15	0.198±0.019	C2
	0.47±0.04	1.52±0.15	-130±20	0.713±0.071	C3
1976	4.59±0.45	0±0	0±0	0.059±0.005	core
(Nov. 2014)	0.83±0.08	0.23±0.02	-159±15	0.107±0.010	X
	1.10±0.11	0.53±0.05	-159±19	0.066±0.006	NC2
	2.45±0.56	0.79±0.07	-154±15	0.147±0.014	NC1
	0.69±0.06	1.06±0.10	-149±14	0.258±0.025	C1
	0.51±0.05	1.54±0.15	-134±17	0.935±0.093	C3
1997	5.90±0.59	0±0	0±0	0.068±0.006	core
(Dec. 2014)	1.33±0.13	0.16±0.01	-162±16	0.115±0.011	NC3
	0.72±0.07	0.48±0.04	-160±16	0.050±0.009	X
	0.95±0.09	0.68±0.06	-158±15	0.108±0.010	NC2
	2.31±0.23	0.84±0.08	-154±15	0.148±0.014	NC1
	0.53±0.05	0.97±0.09	-147±19	0.198±0.019	C1
	0.27±0.05	1.28±0.11	-150±15	0.236±0.023	C2
	0.32±0.03	1.61±0.14	-127±19	0.667±0.066	C3
	0.08±0.02	1.65±0.19	-153±15	0.325±0.032	X

JD' = JD - 2454000,

S : The integrated flux density in the component,

r : The radial distance of the component center from the center of the map,

$\theta$  : The position angle of the center of the component, and

$\phi$  : The FWHM of the component.

Comp<sup>a</sup> : Identification of the individual components. If a component appeared only in a single epoch, we labeled it with X.